

Modelling thrust generation of a two-dimensional heaving airfoil in a viscous flow

By G. C. LEWIN AND H. HAJ-HARIRI

Department of Mechanical and Aerospace Engineering, University of Virginia,
Charlottesville, VA 22904-4146, USA

(Received 25 November 2002 and in revised form 27 May 2003)

A numerical model for two-dimensional flow around an airfoil undergoing prescribed heaving motions in a viscous flow is presented. The model is used to examine the flow characteristics and power coefficients of a symmetric airfoil heaving sinusoidally over a range of frequencies and amplitudes. Both periodic and aperiodic solutions are found. Additionally, some flows are asymmetric in that the upstroke is not a mirror image of the downstroke. For a given Strouhal number – defined as the product of dimensionless frequency and heave amplitude – the maximum efficiency occurs at an intermediate heaving frequency. This is in contrast to ideal flow models, in which efficiency increases monotonically as frequency decreases. In accordance with Wang (2000), the separation of the leading-edge vortices at low heaving frequencies leads to diminished thrust and efficiency. At high frequencies, the efficiency decreases similarly to inviscid theory. Interactions between leading- and trailing-edge vortices are categorized, and the effects of this interaction on efficiency are discussed. Additionally, the efficiency is related to the proximity of the heaving frequency to the frequency of the most spatially unstable mode of the average velocity profile of the wake; the greatest efficiency occurs when the two frequencies are nearly identical. The importance of viscous effects for low-Reynolds-number flapping flight is discussed.

1. Introduction

The oscillation of an airfoil-like appendage – ‘flapping’ – is a common form of propulsion for many animals. Flying animals (birds, bats, insects) generally use flapping to generate both thrust and lift, while many swimming species (fish, aquatic mammals) use flapping primarily to generate thrust. Recently, much effort has gone into the design and construction of devices propelled by flapping, including robotic fish (Triantafyllou & Triantafyllou 1995), ornithopters (Smith 1997), and micro-aerial vehicles (Ashley 1998). One of the primary design challenges in these efforts has been the understanding of the unsteady fluid mechanics of flapping.

The generation of thrust by an oscillating airfoil has a notable effect on the qualitative structure of the wake. Behind a slowly oscillating airfoil, the wake consists of a Kármán vortex street similar to that behind a bluff body; the sense of rotation of the vortices is a result of the momentum deficit behind the airfoil, corresponding to net drag. Conversely, by oscillating the airfoil more energetically, the wake is ‘inverted’ and the vortices have the opposite sense of rotation to that behind a bluff body, indicative of a jet of fluid behind the airfoil and the development of thrust.

Thrust production by an oscillating airfoil was first described in the early part of the twentieth century. Knoller (1909) and Betz (1912) independently noted that the vertical

motion of an airfoil produces an effective angle of attack so that the resulting normal force vector has a component in the forward direction. Later, Katzmayr (1922) made the first experimental observations of this effect and Ober (1925) provided additional theoretical explanations and simple calculations for Katzmayr's results.

Experimentally, Freymuth (1988) demonstrated that an airfoil undergoing either pure pitching or pure heaving is capable of producing thrust. Thrust production due to pitching was also demonstrated by Koochesfahani (1989). Lai & Platzer (1999) and Jones, Dohring & Platzer (1996) used a water tunnel and laser-Doppler velocimetry to obtain high-resolution velocity measurements in the wake of a purely heaving airfoil. Their experimental results confirmed the calculations of Triantafyllou, Triantafyllou & Grosenbaugh (1993), which identified the Strouhal number,

$$St \equiv \frac{fA}{U_\infty}, \quad (1.1)$$

as an important parameter for thrust generation. Here, f is the frequency of oscillation, U_∞ the free-stream velocity, and A is twice the amplitude of motion measured from the mean position (used as the scale for the width of the wake). Lai & Platzer (1999) noted that the structure of the wake (drag or thrust) can be classified according to the Strouhal number, with those motions below a threshold of $St \approx 0.06$ (converted to the current definition of St) producing drag and those above producing thrust. Additionally, at large St ($St > 0.6$), they observed that the wake becomes asymmetric, with the vortex street deflected from the mean position.

Theodorsen (1935) and Garrick (1936) made theoretical calculations of an airfoil undergoing small-amplitude heaving oscillations in an ideal fluid. Their linearized theory showed that all pure heaving motions generate thrust and that thrust is proportional to the square of the frequency. Further, they noted that the propulsive efficiency, defined as the average output power from thrust divided by the average input power, approaches 1.0 as the heaving frequency approaches zero and drops off asymptotically to 0.5 at high frequencies. Others later applied inviscid methods to animal propulsion and extended the theory to include nonlinear effects and large-amplitude motions (Lighthill 1969, 1970, 1975; Chopra 1974, 1976; Chopra & Kambe 1977; Wu 1971). These models again concluded that the propulsion efficiency is maximized as the frequency approaches zero.

Hall & Hall (1996) developed a vortex lattice method to determine the optimal circulation distribution for a prescribed combination of lift and thrust. The method consisted of finding the time-dependent circulation distribution that minimizes induced losses without concern for the details of the mechanics of the flapping motion. This method was later extended by Hall, Pigott & Hall (1998) to include a viscous drag component determined from quasi-steady analysis at each wing station. The model explicitly assumes light wing loading and low reduced frequencies.

Several authors have used lifting-line methods to study flapping flight. Betteridge & Archer (1974) and Archer, Sappupo & Betteridge (1979) developed a method that included twisting of the wing, but excluded unsteady effects of the vortex wake. Philips, East & Pratt (1981) extended the method by modelling the wake using a near component consisting of a vortex sheet and a far component consisting of discrete vortices. Self-induced convection of the wake was neglected, and the method was also limited by low-frequency flapping and inviscid assumptions. Ahmadi & Widnall (1985, 1986) developed a lifting-line method using singular-perturbations and Willmott (1988) developed one using matched asymptotic expansions. Both models were based on linearized equations and were restricted to small transverse oscillations.

Jones, Dohring & Platzer (1998) developed an inviscid model to determine the wake structure on a two-dimensional airfoil undergoing pitching, heaving and combined motions. They noted a favourable comparison between the wake structure predicted by their panel code and the experimentally observed wake for a wide range of St , indicating that the evolution of the wake is primarily an inviscid phenomenon. Average velocity profiles from the model also compared well to experimental results for a wide range of St , although, for low values of St , viscous effects became dominant, and the model could not fully account for the deflected wake at high St . Comparison to total thrust was less accurate because the assumptions used for the simplified momentum integral (e.g. parallel flow, free-stream pressure and insignificant unsteady components) are not valid for such an energetic wake. The panel code was also used to determine the propulsive efficiency over a wide range of heaving parameters. They found that for a given St , the thrust coefficient and efficiency were greatest for low flapping frequency (corresponding to slow flapping with relatively large amplitudes), in agreement with the linear analysis of Garrick (1936). As the frequency was increased, the panel code predicted much lower efficiency than linear theory, which they ascribed to the roll-up of vorticity in the wake. Additionally, Smith, Wilkin & Williams (1996) used the panel method of Katz & Plotkin (1991) to model the flight of a tethered sphingid moth. Their results deviated somewhat from experimental results, most probably due to the inability of the method to account for flow separation. More recently, Liu & Bose (1997) developed a panel method that included spanwise flexibility.

More recently, Minotti (2002) developed a model of a flapping flat plate from two-dimensional potential theory that included a stationary vortex near the leading edge to maintain a regular velocity at the singularity at the leading edge. The model provided reasonable agreement with force measurements by Dickinson, Lehmann & Sane (1999) and Sane & Dickinson (2001).

While contributing significantly to our understanding of flapping propulsion, none of these studies fully addresses the importance of viscous effects, as characterized by an appropriately defined Reynolds number, Re :

$$Re = \frac{U_{\infty}c}{\nu}, \quad (1.2)$$

where c is the chord length and ν the kinematic viscosity. Of course, as the length scales of flapping flight shrink, viscosity will play a greater role in the fluid mechanics. In particular, flow separation becomes much more important as the flapping frequency and amplitude increase. Indeed, experimental observations of flapping insects have revealed that significant leading-edge vortices are generated during the wing-beat (Ellington *et al.* 1996; Willmott & Ellington 1997*a, b*). As demonstrated numerically by Liu *et al.* (1998), these vortices create large low-pressure regions that lead to the high lift coefficients observed in insect flight. It has been theorized that many insects fly at the limit of dynamic stall, where high lift coefficients are generated temporarily after a sudden change in the effective angle of attack.

Gustafson & Leben (1988) and Gustafson (1996) noted the importance of separation effects in hovering flight and identified the importance of vortex ‘splitting’ and ‘shredding’ methods whereby one vortex can be divided or destroyed by another vortex in close proximity; splitting of a leading-edge vortex allows some of the vorticity to be ‘recaptured’ by the airfoil and precludes the loss of lift associated with a stalling airfoil.

As demonstrated theoretically (Streitlien, Triantafyllou & Triantafyllou 1996) and experimentally (Anderson *et al.* 1998), the phasing of interactions between leading- and trailing-edge vortices can greatly affect the thrust and propulsion efficiency of

a flapping airfoil. Optimum efficiency occurs when the leading-edge vortices interact constructively with the trailing-edge vortex, leading to two vortices deposited per flap (Anderson *et al.* 1998).

More fundamentally, Gopalkrishnan *et al.* (1994) characterized the interactions of vortices generated by a flapping airfoil with an oncoming vortex street: vortex amalgamation leading to two vortices being deposited into the wake per cycle or vortex pairing leading to four vortices added per cycle. The amalgamation can be either constructive, leading to stronger vortices and increased thrust, or destructive, enabling energy extraction from the oncoming flow and increasing efficiency. Alternatively, pairing between vortices of opposite sign causes them to drift away from the centreline and results in an expanded wake. Zhu *et al.* (2002) used a panel method to study the three-dimensional vortex interactions of swimming fish and found analogous results. Reviews of current work on fish-like swimming can be found in Pedley & Hill (1999) and Triantafyllou, Triantafyllou & Yue (2000).

Triantafyllou *et al.* (1993) hypothesized that optimal efficiency is obtained when an airfoil is flapped at the frequency of maximum spatial amplification of the wake, based on a linear stability analysis of an average (experimental) jet profile. Using data from the experiments of Koochesfahani (1989) and assuming that the velocity profile is affected weakly by St , they determined that the most unstable mode in the wake occurs from $0.25 \leq St \leq 0.35$. However, they did not consider the dependence on heaving amplitude; in this sense, they determined the optimum frequency for a given amplitude. Experiments in a water tunnel demonstrated that the optimum efficiency fell within the specified range. Further, an extensive literature review showed that many swimming creatures, with a wide variety of morphologies, swim with a Strouhal number within that same range.

Wang (2000) correlated the optimum frequency for heaving airfoils to the time scales of vortex shedding for impulsively started airfoils. For sufficiently large local angles of attack, an impulsively started airfoil will generate net thrust for a short period until a leading-edge vortex is shed. Thus, the normal force vector explanation of Knoller (1909) and Betz (1912) must be modified by the observation that in viscous flows this force is temporally controlled by the shedding of the leading-edge vortex. It was noted that optimum efficiency occurs when the duration of the stroke is just inside the 'thrust window' that exists until the vortex is shed.

The purpose of the present contribution is two-fold: (i) to elucidate the fluid mechanics of low-Reynolds number high-frequency flapping flight, such as on the scale of a large insect, and (ii) to demonstrate correlations between the flow structure and optimization of thrust and flapping efficiency. The paper will concentrate on the heaving of a two-dimensional airfoil, since many of the phenomena of interest (e.g. thrust generation, inversion of the vortex street, leading-edge vortex separation) can be captured with this simple motion. We will reserve studies of pitching and lagging motions for later.

The remainder of this paper is organized as follows: §2 presents the formulation of the problem and describes the governing equations and boundary conditions. Section 3 presents the numerical implementation of the equations. The results are presented in §4 and discussed in §5.

2. Problem definition

Consider a rigid two-dimensional airfoil undergoing prescribed periodic heaving motions at zero angle of attack in an incompressible viscous flow with constant

horizontal (chordwise) free-stream velocity, U_∞ . For computational simplicity, the problem is formulated in a non-inertial reference frame fixed to the airfoil, with the x -axis running parallel to the chord, and the y -axis in the direction of heave. The vertical position of the airfoil in the X, Y inertial frame is denoted by Y_0 .

2.1. Kinematics

For a sinusoidal heaving motion,

$$Y_0 = Y_{max} \sin 2\pi ft,$$

where Y_{max} is the maximum excursion from the mean position. Introducing the reduced frequency, $k = 2\pi fc/U_\infty$, the dimensionless heave amplitude, $h = Y_{max}/c$, and the dimensionless time, $\tau = U_\infty t/c$, the non-dimensional position, \bar{Y}_0 , of the airfoil is

$$\bar{Y}_0 \equiv \frac{Y_0}{c} = h \sin k\tau.$$

Thus, the dimensionless heave velocity can be expressed as $\bar{V}_0 \equiv \partial Y_0/\partial \tau = kh \cos k\tau$. Note that the maximum heave velocity is given by the quantity $kh = 2\pi f Y_{max}/U_\infty$, which differs from the definition of St (equation (1.1)) by a factor of π . Being more intuitive, we prefer to use the quantity kh to categorize the results, although conversion to St will be made when appropriate.

2.2. Governing equations

The formulation requires the modification of the governing equations to account for the apparent body forces on the fluid as observed from the non-inertial reference frame. In the non-inertial frame, the non-dimensional Navier–Stokes equations are written:

$$\frac{\partial \mathbf{u}}{\partial t} = -\nabla p - (\mathbf{u} \cdot \nabla) \mathbf{u} + \frac{1}{Re} \nabla^2 \mathbf{u} - \mathbf{a}_Y, \quad (2.1)$$

where \mathbf{a}_Y is the acceleration of the heaving airfoil. Using the two-dimensional vorticity $\zeta \equiv (\nabla \times \mathbf{u}) \cdot \hat{\mathbf{k}}$ (where $\hat{\mathbf{k}}$ is the unit normal vector perpendicular to the plane of flow), and noting that the curl of the spatially constant quantity \mathbf{a}_Y is zero, (2.1) reduces to

$$\frac{\partial \zeta}{\partial t} = -\nabla \cdot (\mathbf{u}\zeta) + \frac{1}{Re} \nabla^2 \zeta. \quad (2.2)$$

For incompressible flows, the continuity equation can be used to relate the streamfunction, ψ , to the vorticity by:

$$\nabla^2 \psi = -\zeta. \quad (2.3)$$

where the streamfunction, ψ , is defined by $\mathbf{u} \equiv \nabla \times (\psi \hat{\mathbf{k}})$. For convenience, the streamfunction and velocity components are separated into background, Ψ , and disturbance, ψ' , terms so that $\psi = \Psi + \psi'$. The most convenient choice for the background flow is the free-stream velocity, \mathbf{u}_∞ so that

$$\begin{aligned} \mathbf{u}_\infty &\equiv \nabla \times (\Psi \hat{\mathbf{k}}), \\ \mathbf{u}' &\equiv \nabla \times (\psi' \hat{\mathbf{k}}). \end{aligned} \quad (2.4)$$

Thus, $\Psi = U_\infty y + V_0 x$ plus an arbitrary constant taken to be zero. Note that $\nabla^2 \Psi = 0$ and so (2.3) reduces to

$$\nabla^2 \psi = \nabla^2 \psi' = -\zeta. \quad (2.5)$$

That is, the problem has been reduced to an analytical expression for Ψ and two partial differential equations: the familiar vorticity transport equation, (2.2), and a

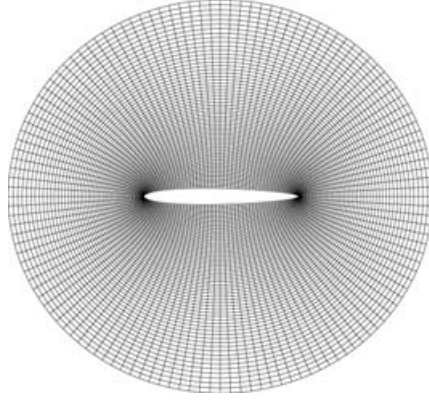


FIGURE 1. Sample airfoil and a portion of the mesh used in the CFD simulations.

Poisson equation for ψ' (2.5). The interaction between these two equations is in the advection term for ζ , which requires the combined background and disturbance velocity. The boundary conditions will also provide an important interaction.

2.3. Boundary conditions

The airfoil is a no-slip surface so that the vorticity at the airfoil, ζ_a , can be related to the total streamfunction by

$$\zeta_a = -\frac{\partial^2 \psi}{\partial n^2} \Big|_{\text{airfoil}} \quad (2.6)$$

where $\partial/\partial n$ refers to the normal derivative. The boundary condition for ψ' at the airfoil is $\psi' = -\Psi$ so that the $\psi = 0$ streamline coincides with the airfoil.

For the infinite-space problem, the appropriate boundary conditions at infinity are that the velocity equals the free-stream velocity and the fluid is irrotational in the inertial frame. The implementation of the truncated outer boundary in the computational domain is discussed below.

3. Numerical implementation

The governing equations are discretized using a conformal map. A rectangular ξ, η domain is first mapped to a circular domain using a log-polar transformation, and the circular cylinder is mapped to an airfoil by means of a Joukowski transformation. The latter is constructed so that the airfoil has no camber but significant radius of curvature at the leading edge and a sharply rounded trailing edge (a cusp is not used to avoid numerical singularities at the trailing edge). Figure 1 shows the airfoil and a portion of a typical mesh (the actual mesh used for the simulations extended about 30 chord lengths out from the airfoil).

The governing equations are transformed from physical (x, y) -space to computational (ξ, η) -space. The vorticity transport equation becomes

$$h_1 h_2 \frac{\partial \zeta}{\partial t} = -(\nabla_{\xi, \eta} \times \psi) \cdot \nabla_{\xi, \eta} \zeta + \frac{1}{Re} \nabla_{\xi, \eta}^2 \zeta, \quad (3.1)$$

where the subscripts $\nabla_{\xi, \eta}$ refer to derivatives in the ξ, η domain. h_1 and h_2 are the grid transformation metrics which relate the size of a grid cell in the (x, y) -domain to the (ξ, η) -domain.

The Poisson equation for ψ' becomes

$$\nabla_{\xi,n}^2 \psi' = -h_1 h_2 \zeta. \tag{3.2}$$

3.1. *Boundary conditions*

Boundary conditions are required for ζ (equation (2.2)) and ψ' (equation (2.5)). At the airfoil, (2.6) is discretized using a second-order difference equation:

$$\zeta_a = \frac{(\psi_2 - 8\psi_1 + 7\psi_0)}{2\Delta n^2}.$$

At the inlet, the flow is assumed to be irrotational. At the outlet, viscous effects are neglected so that the material derivative of the vorticity vanishes. For the streamfunction, $\psi' = -\Psi$ on the airfoil, as noted previously. At the outer boundary, the normal derivative of ψ' is prescribed, which amounts to specifying the tangential velocity. At the inlet, disturbances to the free-stream flow are neglected so that

$$\left. \frac{\partial \psi'}{\partial n} \right|_{inlet} = 0. \tag{3.3}$$

Because the wake is highly unsteady, a much more ‘passive’ boundary condition must be developed for the outlet. If viscosity is again neglected, then the material derivative of velocity is affected only by the pressure gradient. In general, these pressure gradients will be small, and are also neglected. Thus, at the outlet

$$\left. \frac{D}{Dt} \left(\frac{\partial \psi'}{\partial n} \right) \right|_{outlet} = 0, \tag{3.4}$$

which has a similar form to boundary condition for vorticity and allows for some simplification of the numerical procedure. In practice, the simulations are terminated before any significant vorticity becomes close to the outlet boundary.

3.2. *Discretization*

For spatial differencing of the vorticity transport equation, fourth-order centred-differencing is used for the viscous terms, while a third-order upwind scheme is used for the advection terms. Stepping in time is performed using a second-order Runge–Kutta scheme. For the Poisson equation for streamfunction, the equations are discretized using a fourth-order centred scheme and solved using a multi-grid solver.

3.3. *Forces*

The total force on the airfoil is a combination of pressure and viscous forces. A simplified procedure for calculating the pressure on the airfoil is based on the relationship

$$\frac{\partial p}{\partial s} = -\frac{1}{Re} \frac{\partial \zeta}{\partial n} + \mathbf{a} \cdot \mathbf{ds}, \tag{3.5}$$

which relates the pressure gradient along a no-slip wall to the normal derivative of vorticity, modified for the non-inertial reference frame (see equation (2.1)). The pressure force at every point on the airfoil is found by assuming an arbitrary value of pressure at one point (the trailing edge) and marching through successive grid points using (3.5).

The viscous force is found from the shear stress on the airfoil, τ_s , which is related to the tangential velocity, u_s , by

$$\tau_s = \frac{1}{Re} \frac{\partial u_s}{\partial n} = -\frac{1}{Re} \zeta_a. \tag{3.6}$$

Once the pressure and viscous forces are known at each point, they are integrated numerically to find the total force components, F_X and F_Y , and moment, M , on the airfoil.

3.4. Power

The instantaneous power can be calculated from the total force by multiplying the force components by the appropriate velocity components in the inertial frame. The input power coefficient is the power needed to heave the airfoil, $P_i = F_Y V_0$. Note that the power input is negative by this definition. The output power coefficient from thrust is $P_o = -F_X U_\infty$, so that the output power is positive when thrust is produced and negative for drag.

Integrating the instantaneous power yields the total work required to heave the airfoil, W_i , and the work done in propelling it, W_o . The ratio of total work out to work in is the thrust efficiency, $\eta = -W_o/W_i$. Note that η ranges from $-\infty$ for steady (non-heaving) flight to 1.0 for theoretically perfect efficiency.

3.5. Initial conditions and code validation

Inviscid solutions were used as the initial conditions for all simulations. Using a viscous steady-flow solution had no effect on the long-term solutions. Validation and convergence studies of the code are presented in Appendix A.

4. Results

4.1. Flow patterns

The numerical model described above is used to simulate a heaving airfoil with frequencies ranging from $2.0 \leq k \leq 10.0$ and maximum heave velocities from $0.8 \leq kh \leq 1.5$ ($0.25 \leq St \leq 0.48$) at $Re = 500$. A wide variety of flow patterns are observed in the parameter space studied. The long-term solutions for flows with $kh = 0.8$ are periodic and symmetric, meaning each upstroke and downstroke are mirror images. For $kh = 1.0$, asymmetric solutions are observed. For $kh \geq 1.2$, aperiodic, quasi-periodic, and asymmetric solutions are common.

The term *aperiodic* is self-explanatory; by *quasi-periodic* we mean that for several periods the flow changes relatively little from period to period until there is a large qualitative change lasting for a few strokes, after which the flow returns to its former slowly evolving state. *Asymmetric* solutions are those where there is no symmetry in either the forces on the airfoil or the vorticity in the wake in the direction of heaving, as when the wake is deflected from the mean heave position.

The reduced frequency, k , is the primary factor governing the topology of the leading-edge vortex (LEV), with kh being a secondary factor. For low k , the LEV separates and advects downstream, where it often interacts with the trailing-edge vortex (TEV). As k increases, the vortex separates later in each stroke until, instead of advecting downstream, it is stretched and dissipated by the nascent LEV on the subsequent stroke. For high kh there is a transition region of aperiodic flows where some LEVs are shed and others are dissipated. Further, for high k and kh , the LEV can circumnavigate the leading edge to the other side of the airfoil and advect downstream either in the free stream or within the boundary layer on that side.

Figure 2 outlines the type of flow observed for each simulation as a function of frequency, k , and maximum heave velocity, kh . Representative examples of each flow regime will be discussed below.

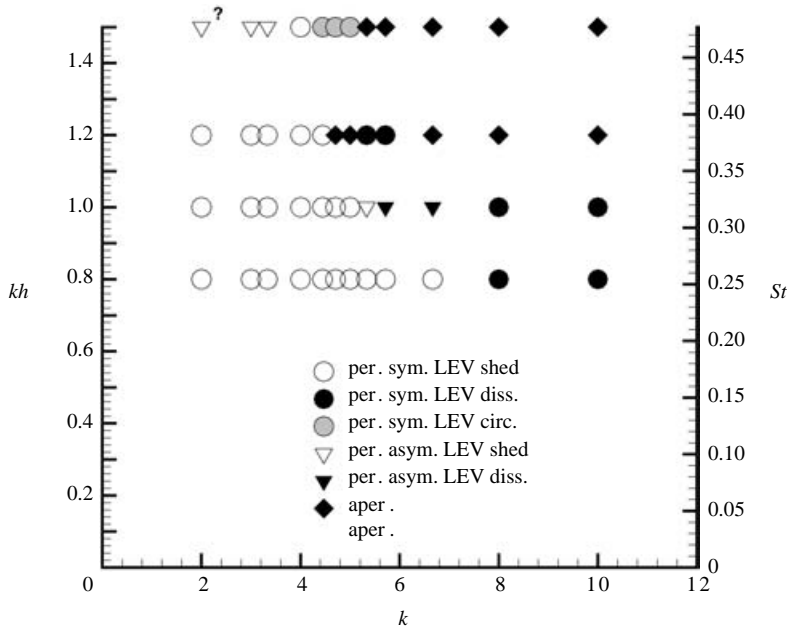


FIGURE 2. Qualitative results for all simulations, based on k and kh . per. = periodic; aper. = aperiodic; sym. = symmetric; asym. = asymmetric; LEV shed = LEV shed into flow; LEV diss. = LEV dissipated by interaction with the leading edge/nascent LEVs; LEV circ. = LEV circumnavigates the leading edge and is shed on the other side.

4.1.1. $kh = 0.8$ ($St \approx 0.25$)

For $kh = 0.8$ all simulations produce periodic and symmetric results. Figure 3 shows the vorticity contours for the downstroke of a simulation at $k = 2.0$. During the first half of the stroke, vortex filaments form at both the leading and trailing edges. At the leading edge, the vortex filament begins to roll up into a vortex at mid-stroke and the nascent LEV continues to be fed by this filament for the second half of the stroke. As the airfoil motion reverses, the vortex filament weakens and a significant secondary vortex extends from the airfoil, cutting off the filament feeding the LEV. The LEV then advects downstream.

The fate of the LEV can be determined by observing the LEV created during the previous upstroke, which is underneath the airfoil near mid-chord at the start of the downstroke (because the flow is symmetric for this case, the upstroke is a mirror image of the downstroke). The LEV advects downstream where interaction with the trailing edge cuts off the vortex filament emanating from the trailing edge that formed at the start of the downstroke. After the LEV passes, the vortex filament reforms for the remainder of the stroke and feeds the passing LEV. Within three chord lengths downstream, the LEV, its secondary vortex, and the TEV coalesce into a single vortex.

As the heaving frequency increases, the time scale of the heaving motion approaches the hydrodynamic time scale of the flow. At $k = 3.333$, the two time scales are nearly equal and the LEV reaches the trailing edge just as the TEV (with opposite sense of rotation) is beginning to form. As shown in figure 4, the LEV is entrained in the nascent TEV and only one vortex, a much weakened TEV, is deposited into the wake per stroke.

As the frequency increases further, the LEV remains near the leading edge for a larger portion of the subsequent stroke where its strength is reduced substantially by

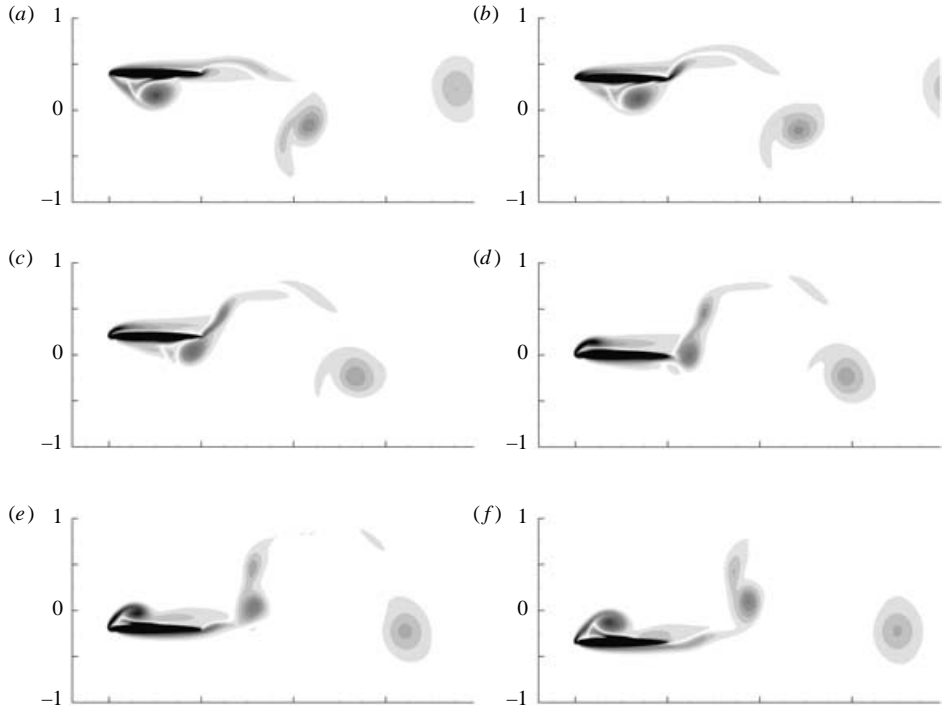


FIGURE 3. Simulated vorticity field for the downstroke of a heaving airfoil with $k=2.0$, $kh=0.8$. Contours are evenly spaced at $\zeta = \pm(2, 6, 10, \dots)$ with the sign determined by the sense of rotation.

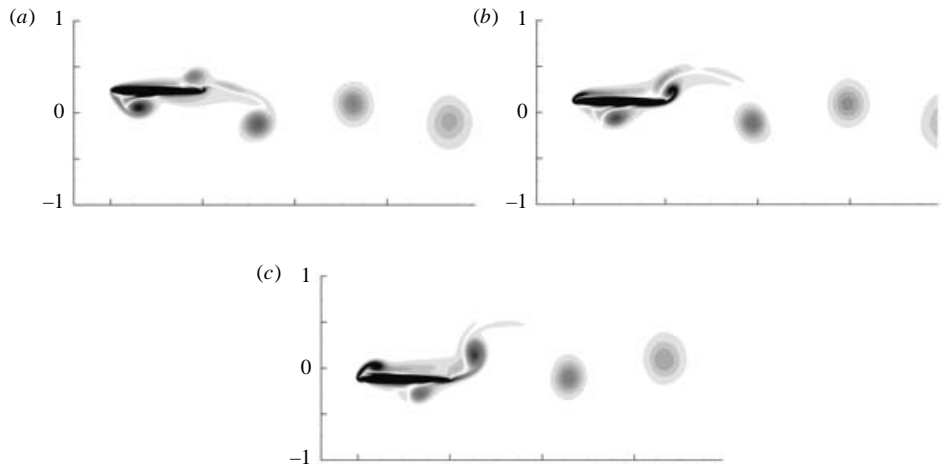


FIGURE 4. Simulated vorticity field for the downstroke of a heaving airfoil with $k=3.333$, $kh=0.8$. Contours are evenly spaced at $\zeta = \pm(2, 6, 10, \dots)$ with the sign determined by the sense of rotation.

interaction with the airfoil. Figure 5 shows the vorticity field for the downstroke of a simulation with $k=6.667$. Notice that the LEV from the previous upstroke remains stationary underneath the airfoil near the quarter-chord point for a substantial portion of the stroke (again, the flow is symmetric). During this time it partially dissipates

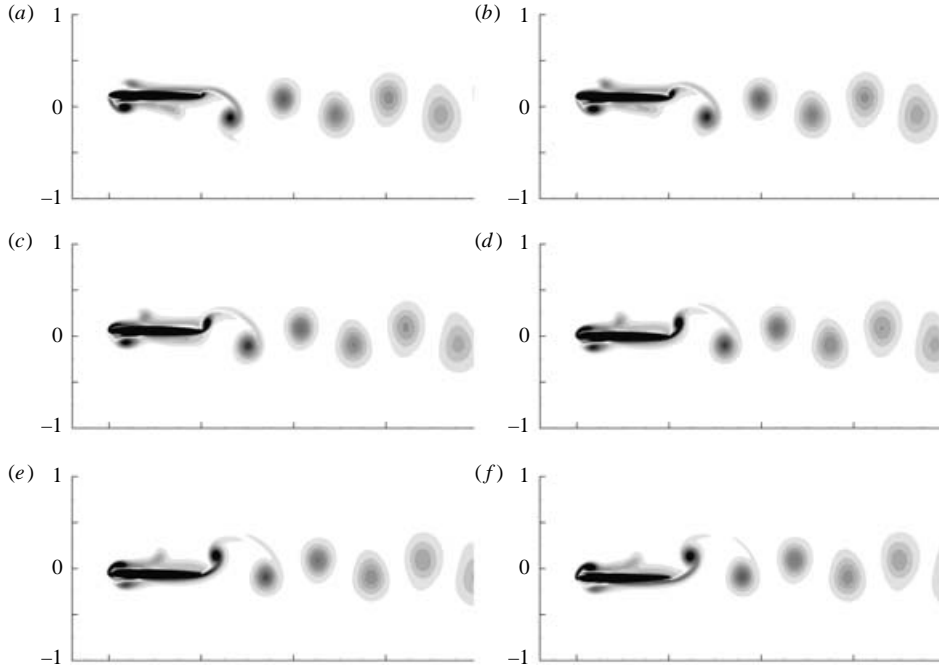


FIGURE 5. Simulated vorticity field for the downstroke of a heaving airfoil with $k=6.667$, $kh=0.8$. Contours are evenly spaced at $\zeta = \pm(2, 6, 10, \dots)$ with the sign determined by the sense of rotation.

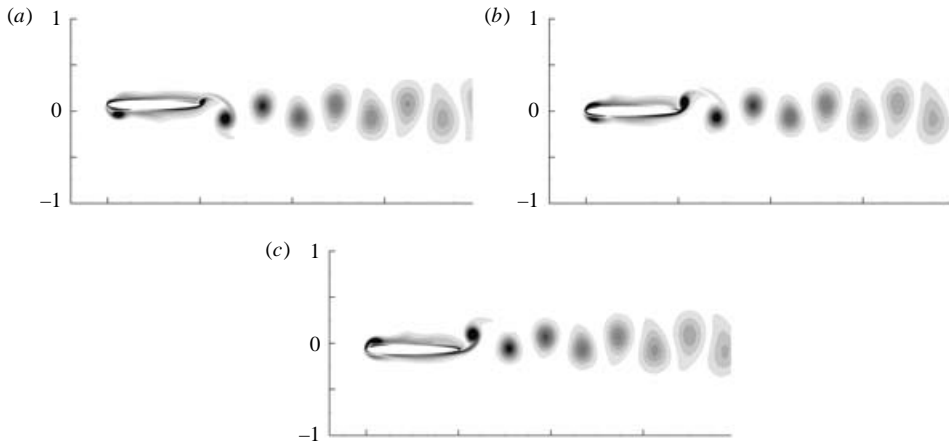


FIGURE 6. Simulated vorticity field for the downstroke of a heaving airfoil with $k=10.0$, $kh=0.8$. Contours are evenly spaced at $\zeta = \pm(2, 6, 10, \dots)$ with the sign determined by the sense of rotation.

before moving along the underside of the airfoil. The remnants of the LEV shed from an earlier upstroke can be seen underneath the airfoil near the two-thirds chord point. This remnant ‘spills over’ the trailing edge on the downstroke and reinforces the growing TEV.

Figure 6 shows a sequence for $k = 10.0$. Note, however, that the LEV produced on the previous upstroke is stretched partially around the leading edge on the

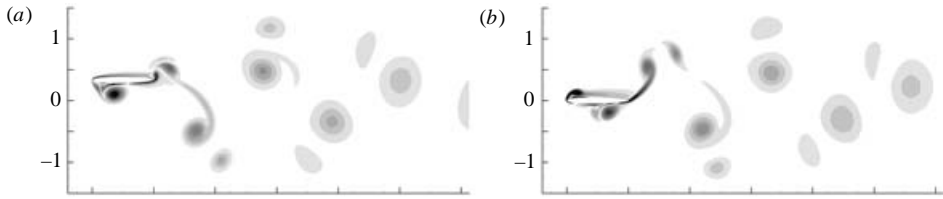


FIGURE 7. Simulated vorticity field for the downstroke of a heaving airfoil with $k=3.0$, $kh=1.0$. Contours are evenly spaced at $\zeta = \pm(2, 6, 10, \dots)$ with the sign determined by the sense of rotation.

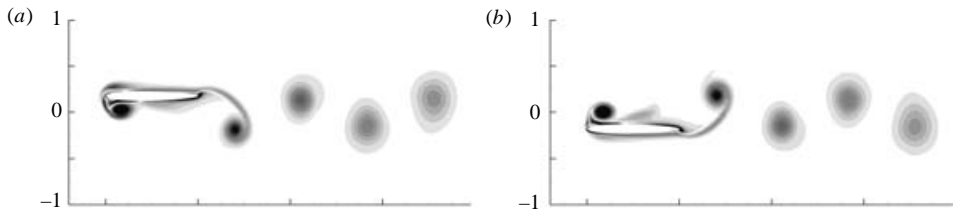


FIGURE 8. Simulated vorticity field at the upper and lower limits of motion for a heaving airfoil with $k=5.714$, $kh=1.0$. Contours are evenly spaced at $\zeta = \pm(2, 6, 10, \dots)$ with the sign determined by the sense of rotation.

downstroke, and is almost entirely dissipated – vortex ‘shredding’ to use the terminology of Freymuth (1985).

4.1.2. $kh = 1.0$ ($St \approx 0.32$)

For $kh = 1.0$, the simulation at $k = 2.0$ is similar to that of the previous section. At $k = 3.0$, however, the LEV pairs up with the TEV, but the two do not immediately merge. Thus, four vortices are shed into the wake with each flap and the wake is much wider than it is in the other cases, much like the expanding wake of Gopalkrishnan *et al.* (1994). As seen in figure 7, the LEV, being much weaker than the TEV, revolves around the TEV until it is stretched and shredded between successive TEVs. At $k = 3.333$, the vortices again interact destructively, and only two vortices are shed per flap, as in the previous section.

In the mid- to high-frequency range, a noticeable asymmetry develops. At $k = 5.0$, the flow is symmetric, with the LEV separating and advecting downstream. At $k = 5.714$, however, the LEV produced on the upstroke is stretched around the LEV of opposite orientation on the subsequent downstroke. The stretching of the LEV produced on the downstroke is much less intense, and a significant vortex is carried downstream. Figure 8 shows a comparison between the vorticity fields at the upper and lower extremes of the heaving motion.

The asymmetry in the flow leads to an asymmetry in the power coefficients, as well. Figure 9(a) shows the average power coefficients for each stroke for the same simulation. The coefficients are periodic, but more power is output during the downstroke than during the upstroke. After the initial start-up of the airfoil, the asymmetry stabilizes and persists for the duration of the simulation. Asymmetric solutions are found until $k \geq 8.0$, where the leading-edge vortices on both strokes are again stretched and dissipated equally.

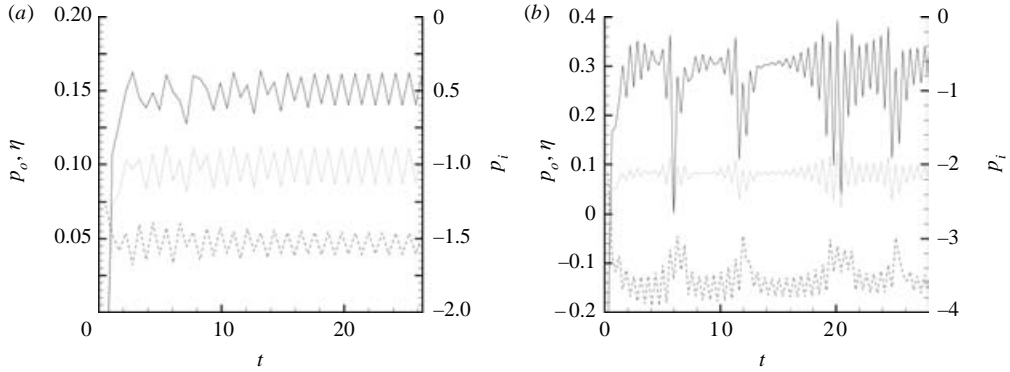


FIGURE 9. Average power coefficients for each stroke for a simulation of a heaving airfoil with (a) $k = 5.714$, $kh = 1.0$; (b) $k = 10.0$, $kh = 1.2$. Each point represents the average over the stroke ending at the time indicated on the horizontal axis. — —, input power; —, output power; ···, efficiency.

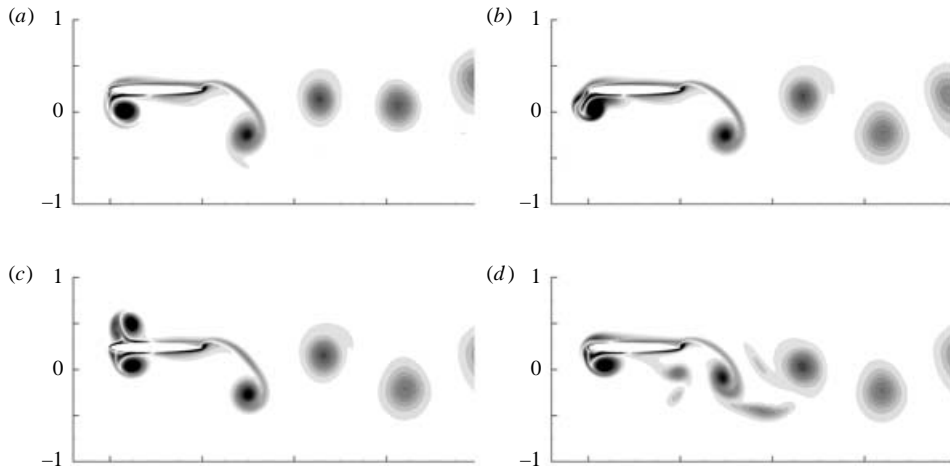


FIGURE 10. Simulated vorticity field for subsequent strokes of a heaving airfoil with $k = 5.0$, $kh = 1.2$. Each snapshot is taken at the upper extreme of the heaving motion to show the aperiodic nature of the wake. Contours are evenly spaced at $\zeta = \pm(2, 6, 10, \dots)$ with the sign determined by the sense of rotation.

4.1.3. $kh = 1.2$ ($St \approx 0.38$)

For $kh = 1.2$, the simulations at low frequency are similar to those of the previous sections, with the exception of a significant, transient wake deflection at $k = 2.0$. In the intermediate frequencies, aperiodic solutions are found. At $k = 4.444$, the flow is symmetric and periodic, and the LEV separates and advects downstream, similarly to the cases at lower kh . At $k = 5.333$, the flow is also symmetric and periodic, but the LEV is stretched around the leading edge and dissipated. Between these frequencies, however, the flow is aperiodic, with some LEVs being dissipated and some being advected downstream. Figure 10 shows the variation of the vorticity field for subsequent periods at $k = 5.0$. Residual vorticity from previous heaving motions leads to small variations in the location of the LEV during its formation which lead to qualitatively large changes in the flow. This phenomenon persists for the duration of the simulation.

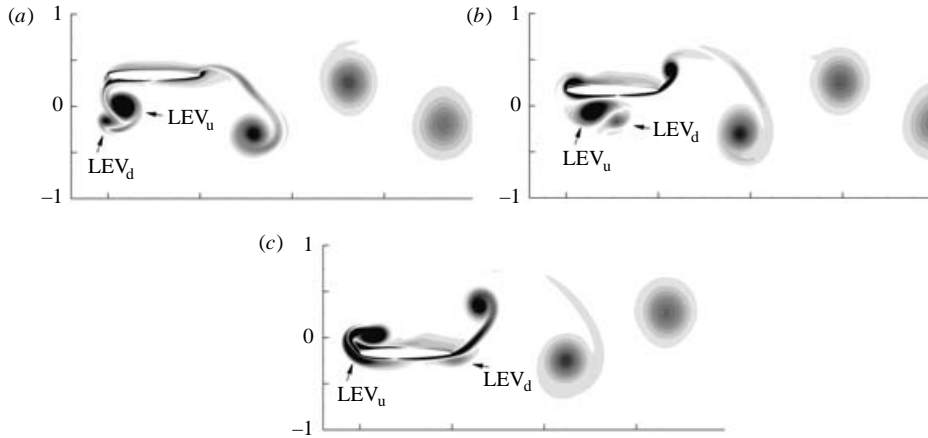


FIGURE 11. Simulated vorticity field for the downstroke of a heaving airfoil with $k = 4.444$, $kh = 1.5$. Contours are evenly spaced at $\zeta = \pm(2, 6, 10, \dots)$ with the sign determined by the sense of rotation.

For $k \geq 6.67$, the flows are quasi-periodic in that the position of the LEV from period to period changes very little until all of a sudden it is forced around the leading edge of the airfoil and is advected downstream on the other side, reminiscent of a relaxation oscillation. The phenomenon is most pronounced for $k = 10.0$. Figure 9(b) shows the average power coefficients and efficiency for each stroke for this case. The envelope of the force curve clearly demonstrates the relaxation oscillation nature of the phenomenon.

4.1.4. $kh = 1.5$ ($St \approx 0.48$)

At $kh = 1.5$, the deflected wake at $k = 2.0$ persists for significantly longer than it does at $kh = 1.2$. Analysis of the forces on the airfoil and the vorticity field show that the asymmetry in the vertical forces and the deflection angle of the wake vortices are decreasing monotonically. It was not feasible to continue the simulation to determine if the long-term solution has a deflected wake, although it appears that the solution will eventually become symmetric.

The intermediate frequencies differ from the cases where $kh = 1.2$ in that instead of the LEVs being stretched around the leading edge, they circumnavigate the leading edge and are shed into the flow on the opposite side of the airfoil. Figure 11 shows a series of snapshots for the downstroke from the simulation with $k = 4.444$. In the first frame, the LEV created on the previous downstroke (LEV_d) has circumnavigated the leading edge and is paired up with the vortex created on the just completed upstroke (LEV_u). In the second frame, LEV_d continues to move around LEV_u . In the final frame (near the end of the downstroke), the two LEVs have separated owing to interaction with the airfoil, with LEV_d moving downstream along the airfoil. LEV_u is beginning to circumnavigate the leading edge and the process is repeated on each subsequent stroke.

At high frequencies, the flows are highly aperiodic with large wake deflections. Figure 12 shows two vorticity snapshots from a simulation with $k = 10.0$. The direction in which the wake is deflected is observed to switch from upward to downward (a similar phenomenon occurs at $k = 8.0$). This switching was reported by Jones *et al.* (1998) for high-frequency heaving in water-tunnel experiments, although they were not able to demonstrate switching in their inviscid (panel method) modelling. To

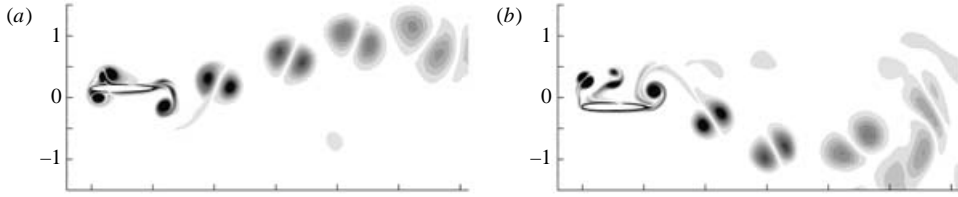


FIGURE 12. Simulated vorticity field for a simulated heaving airfoil with $k = 10.0$, $kh = 1.5$ showing switching of deflected wake. Contours are evenly spaced at $\zeta = \pm(2, 6, 10, \dots)$ with the sign determined by the sense of rotation.

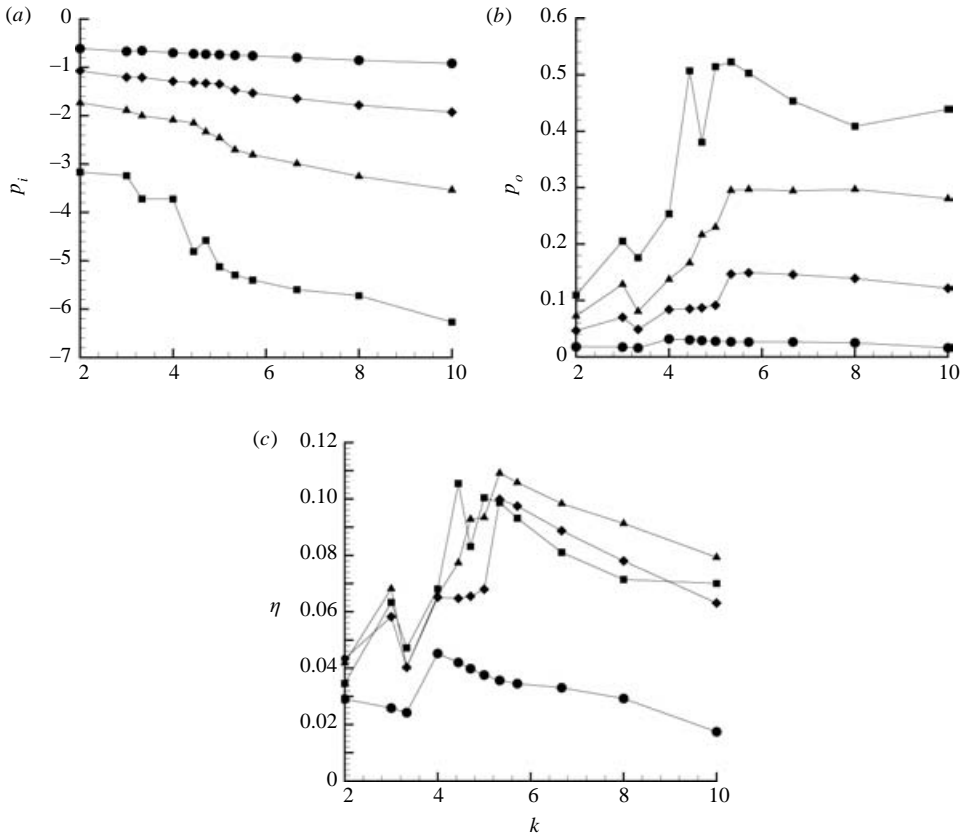


FIGURE 13. Average input (a) and output (b) power and average efficiency (c) for each simulation: \bullet , $kh = 0.8$ ($St \approx 0.25$); \blacklozenge , 1.0 ($St \approx 0.32$); \blacktriangle , 1.2 ($St \approx 0.38$); \blacksquare , 1.5 ($St \approx 0.48$).

our knowledge, this is the first report of a numerical simulation that reproduces this phenomenon.

4.2. Efficiency

4.2.1. Power and efficiency

Figure 13 shows the average power components and efficiency for each of the simulations. Because many of the simulations produce aperiodic solutions, averages were taken over many flaps (starting after several flaps had been made to allow for the suppression of the initial transients). The overall efficiency is very low: $\eta_{max} \approx 11\%$ at

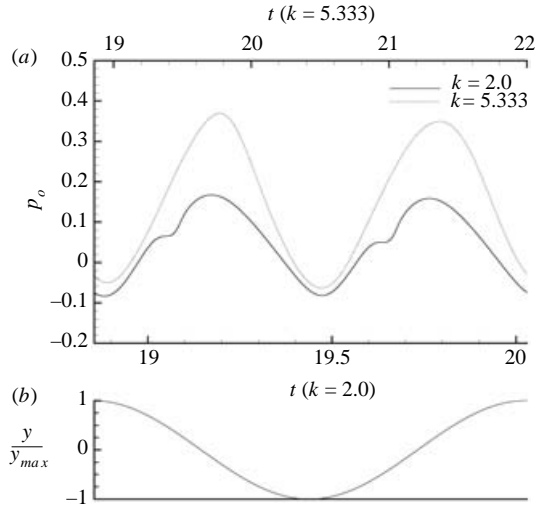


FIGURE 14. (a) Output power for $k = 2.0$ and $k = 5.333$ ($kh = 1.0$) over one heaving cycle. (b) The vertical position, Y/Y_{max} , of each airfoil in its respective flap.

$k = 5.333$ and $kh = 1.2$. In comparison, Wang (2000) found the maximum efficiency for a thin ellipse to be $\approx 10\%$ at similar values of frequency and amplitude.

The trends in heaving efficiency can be linked to the flow structure; in particular, the evolution and fate of the LEV noticeably affects the forces on the airfoil and the efficiency. For $kh \geq 1.0$, the substantial jump in efficiency in the intermediate frequencies corresponds directly to the transition from a shed LEV to one that is dissipated. This correlation is not observed for $kh = 0.8$, but it is noted that for $kh = 0.8$ not only is the overall efficiency extremely poor ($\eta \leq 4.5\%$), but the transition from shed to dissipated LEVs is gradual.

Additionally, the comparatively low efficiency observed at $k = 3.333$ for all kh in this study corresponds directly to the negative interference at the trailing edge between the LEV and the TEV of opposite sign (see figure 4, for example).

Figure 14 shows the horizontal (output) power components for two different simulations with $kh = 1.0$: $k = 2.0$ (low efficiency) and $k = 5.333$ (high efficiency). The horizontal axes are scaled by the appropriate k so that the strokes from each simulation coincide. For the $k = 5.333$ case, the output power rises and falls smoothly and is roughly correlated with the velocity of the airfoil; peak power occurs when the airfoil is near the mid-stroke and is lowest when the airfoil is near the extremes. For the $k = 2.0$ case, the output power initially rises at the start of each stroke but before the airfoil reaches mid-stroke, the power temporarily levels off, after which it remains substantially below the $k = 5.333$ case. This 'dip' in power corresponds directly to the separation of the LEV.

At high frequencies, the efficiency slowly tapers off as k increases for all kh , mimicking the theoretical calculations for inviscid heaving airfoils. (A direct comparison is not practical, as viscous effects reduce the thrust on the airfoil substantially.) Interaction between the airfoil and the shed vortices induces a drag on the airfoil, which has a stronger effect at higher frequencies owing to the greater proximity of the vortices. In addition, for high values of kh , the wakes are highly energized by the deposition of many vortices (LEVs, TEVs, and secondary vortices) into the flow. Much of this energy does not go towards providing useful work (thrust) and is thus wasted.

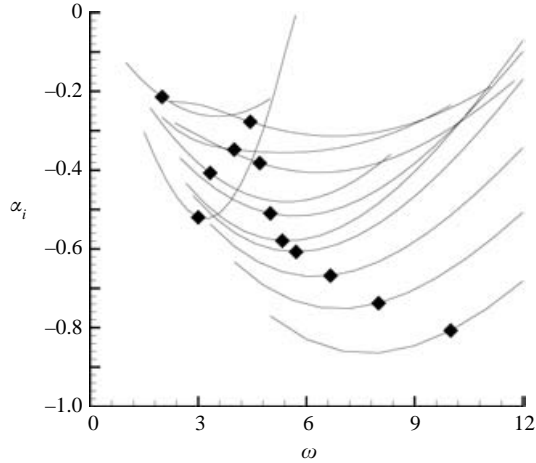


FIGURE 15. Imaginary component of the most unstable modes for simulations with $kh = 1.0$. The diamonds indicate the heaving frequency used to obtain each velocity profile.

Finally, whether or not a flow is periodic appears to have little effect on the propulsive efficiency. For example, the simulations with $k = 4.444$ and $k = 5.0$ at $kh = 1.2$ are aperiodic, with efficiencies intermediate to the periodic cases with $k = 4.0$ and $k = 5.333$. Additionally, the simulated flow $k = 5.333$ and $kh = 1.5$ is aperiodic but the efficiency is only slightly less than the periodic case at $k = 5.0$.

4.2.2. Linear stability analysis

Following Triantafyllou *et al.* (1993), the most unstable spatial mode for the average horizontal velocity profiles for each of the simulations are determined (see Appendix B). These velocity profiles clearly account for the effect of heaving amplitude. The velocity profiles are calculated one chord length downstream of the trailing edge, and the (small) vertical components are neglected. The spatial growth rate of the most unstable mode (the most negative imaginary part of the wavenumber) is calculated as a function of real frequency, ω , and plotted to determine the frequency corresponding to the maximum spatial amplification. Figure 15 shows the relationship between ω and the imaginary part of the wavenumber, α_i , for the most unstable mode for each of the simulations at $kh = 1.0$. Each curve in this figure is identified by the heaving frequency, k , used to obtain each velocity profile.

Most of the curves are nested in an orderly way within one another; a few deviate noticeably. The curve determined from the simulation with $k = 3.0$ is shifted towards lower values of ω and has a much larger (negative) imaginary part than expected from the general trend. Additionally, the curves calculated from the simulations at $k = 4.444$ and $k = 4.706$ have smaller (negative) imaginary parts than expected and are shifted towards the higher frequencies. These shifts can be correlated to the qualitative shape of the velocity profiles (shown in figure 16). Whereas most of the profiles show a sharp peak in the velocity at the mid-line, the velocity profile for the $k = 3.0$ case is much broader, as expected for the expanding wake produced in this simulation. The profiles for $k = 4.444$ and $k = 4.706$ show significant ‘hips’ above and below the main velocity jet.

There is a strong correlation between heaving efficiency and the separation between the heaving frequency for a given profile and the frequency resulting in the maximum spatial amplification of this profile. The highest efficiencies for $kh = 1.0$ occur at

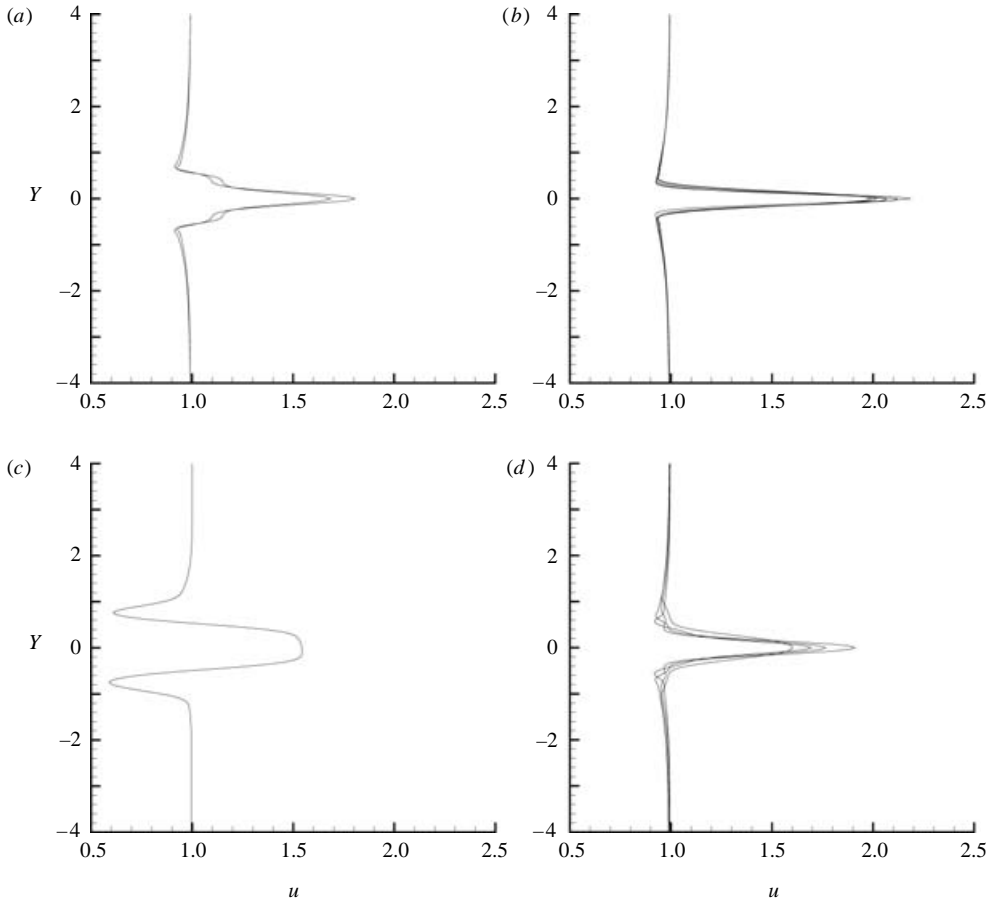


FIGURE 16. Average velocity profiles for simulations with $kh = 1.0$. (a) $k = 4.444, 4.706$; (b) $k \geq 5.333$; (c) $k = 3.0$; (d) other.

$k = 5.333$ and $k = 5.714$, where the airfoil is driven almost exactly at the most unstable frequency. As the heaving frequency increases, the driving frequency becomes greater than the frequency of the most unstable mode. Similarly, for low-frequency heaving, the driving frequency is lower than the frequency of the most unstable mode, with the notable exception of the case where $k = 3.0$. Here, the driving frequency is again very near the frequency of the most unstable mode. While this does not correspond to the global maximum efficiency, it does correspond to a substantial local maximum efficiency, as seen in figure 13. Similar results were found for each value of kh .

5. Discussion

Over the parameter ranges covered in this numerical study, several distinct solution topologies are observed, including aperiodic and asymmetric solutions. In their comprehensive experimental investigation of flow around an oscillating cylinder, Williamson & Roshko (1988) identified a number of different flow regimes similar to those observed in this work, including deflected wakes as well as various numbers of vortices shed into the wake per oscillation, symmetrically or asymmetrically. Additionally, for a large portion of their parameter space, they found no stable pattern.

We find that the wake patterns depend primarily on the fate of the LEV: whether or not it is shed, and how it interacts with the TEV. When shed, the LEV can either reinforce (positively or negatively) the TEV, resulting in two vortices shed into the wake per flap, or it can pair up with the TEV, resulting in four vortices shed per flap. This finding is in agreement with Gopalkrishnan *et al.* (1994) for interactions with oncoming vortex streets.

Whereas Williamson & Roshko (1988) found sharp changes between the various flow regimes in their study of a circular cylinder, the results here demonstrate that for a heaving airfoil the transition regions are often characterized by aperiodic flows that 'switch' between the neighbouring flow regimes. Additionally, at high kh and high k , all of the simulations produced aperiodic results. As noted, the aperiodic nature of the flows can be traced to the topology of the LEV; small secular effects cause large changes in the dynamics of the LEV.

The fate of the LEV can also be correlated to the heaving efficiency. While the overall efficiency was low, large increases in efficiency occur at the transition from a shed LEV to one that is dissipated. Wang (2000) noted that the heaving frequency needed for maximum efficiency should correspond to the period with which vortices are shed from impulsively started airfoils, since this shedding causes the forces on the airfoil to drop substantially. Indeed, it is confirmed here that the timing of the separation of the LEV is crucial to the heaving efficiency, with a significant gain in efficiency occurring when the LEV remains attached for the duration of each stroke. The results are also in accordance with Gustafson & Leben (1988) and Gustafson (1996) in that some of the vorticity contained in the LEV is subsequently recaptured by the airfoil.

In agreement with Anderson *et al.* (1998), high thrust coefficients and propulsion efficiencies correspond to the positive reinforcement of the TEV by the LEV. Additionally, thrust and efficiency are greatly reduced when there is negative reinforcement between the LEV and TEV. This differs from Gopalkrishnan *et al.* (1994), who noted that energy extraction occurs when airfoil-generated vortices negatively interact with an oncoming vortex street. However, the primary source of upstream vorticity was a separate bluff body, which allowed energy extraction independent of vortex creation. Because the interaction in this study is with vortices produced at the leading edge of the same airfoil, no net energy extraction can occur.

The results presented here also differ from the results of Zhu *et al.* (2002), who found that the propulsive efficiency of a 'robo-tuna' in an inviscid model was increased when negative reinforcement of vortices occurred. In this case, the upstream vorticity was created by a different hydrodynamic surface on the same structure (dorsal *vs.* tail fins). Similarly, Tuncer & Platzer (1996) noted that a large increase in efficiency is possible when a stationary airfoil is placed in the wake of a heaving airfoil. In each of these cases, instead of wasting the energy contained in the vortices created by an upstream structure, the energy is partially recaptured by the downstream structure. Because the current model includes only a single airfoil, energy recapture in this sense is not possible.

At higher frequencies, the comparatively slow tapering off of efficiency with increased k is reminiscent of efficiency curves predicted by ideal flow models (Garrick 1936; Jones & Platzer 1997; Jones *et al.* 1998). As the heave frequency is increased, the wavelength of the wake vortices is shortened and shed vortices remain nearer to the trailing edge for a greater portion of each flap, and the increased interaction leads to lower efficiency (Jones & Platzer 1997). Note that for high-frequency flapping, the flow is most like an inviscid flow in that vorticity is shed primarily from the trailing

edge. The analogy does not strictly hold for high kh , however, as the LEV and its secondary vortices are occasionally shed into the wake.

In direct contrast to ideal flow models, the maximum efficiency is found at an intermediate frequency. Whereas ideal flow models approach maximum efficiency as $k \rightarrow 0$, our simulation (and others) shows that the early separation of the LEV as k decreases past a (kh dependent) threshold frequency results in a large decrease in thrust forces and efficiency.

While the current study focuses solely on heaving motions, it is expected that analogous relationships will hold for motions with pitching and lagging. With pitching, the behaviour and evolution of the LEV can be controlled much better. Larger amplitudes and lower frequencies can be achieved without the premature separation of the LEV and subsequent drop in forces on the airfoil. Indeed, experimental and computational studies of insect flight demonstrate that the LEV remains attached to the leading edge of the wing for the majority of the stroke and is shed by rapid pronation or supination at the end of each stroke (Liu *et al.* 1998; Ellington *et al.* 1996). Additionally, for a real wing a major contributor to the LEV remaining attached is the axial flow along the three-dimensional LEV. Absent that in two-dimensions, the pitching of the wing will assist in the streamlining of the motion and control of the LEV.

This work was supported in part by NASA Grant NAG-1-01120, a fellowship from the Virginia Space Grant Consortium (G.C.L.), and the John H. and Dorothy W. Sidebottom and Carlos A. and Esther H. Farrar Fellowships from the University of Virginia (G.C.L.).

Appendix A. Validation of the code

The performance of the model was assessed through several test simulations. Preliminarily, flow around a stationary circular cylinder was simulated at $Re = 100$ using a 128×384 grid. The simulated St was 0.164 and the force coefficients on the cylinder were found to be $C_{D,avg} = 1.31$, $C_{L,rms} = 0.226$ and $C_{L,max} = 0.319$, all of which agree well with published numerical and experimental results (see Tritton 1959; König, Eisenlohr & Eckelmann 1990; Zhang *et al.* 1995; Tang & Aubry 1997, for example).

To assess the dynamics of the vortex wake, the simulated flow behind an impulsively started cylinder was compared to the experimental results of Bouard & Coutanceau (1980). Figure 17(a) shows the evolution with time of the closed wake length, L , and the coordinates of the main eddy core, X_e , Y_e , for $Re = 550$. Given the three-dimensional nature of the experimental problem and the difference in starting conditions, the agreement is very good.

Additionally, the computational and experimental velocities along the mean wake line were compared for the same flow conditions as above. Figure 17(b) shows a comparison between computed and experimental flows. Again, the agreement is very good.

To ascertain the effects of grid refinement on the solution, a heaving airfoil was simulated with $k = 4.0$, $h = 0.25$ and $Re = 1000$ using a number of grids. Figure 18 shows the vorticity at the leading and trailing edges after one stroke for various levels of grid refinement (where the relative grid spacing of 1 corresponds to a 512×512 grid). The theoretical solution at zero grid spacing as calculated by Richardson extrapolation is also plotted. The leading and trailing regions are chosen because they

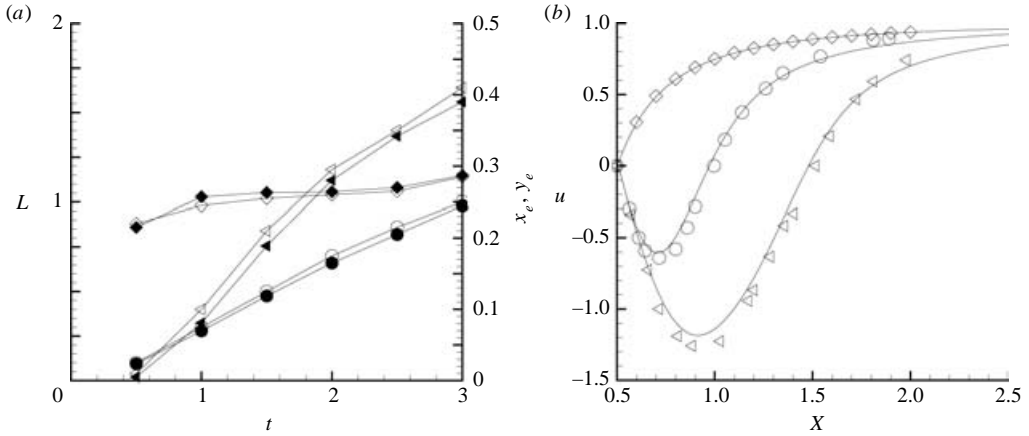


FIGURE 17. (a) Comparison of numerical (solid symbols) and experimental (open symbols) lengths of the closed wake, L , and location of the main eddy core, X_e, Y_e (measured from the most downstream point of the cylinder): \circ , L ; \triangleleft , X_e ; \diamond , Y_e . (b) Comparison of simulated (—) velocity at the mean line of the wake with the inviscid solution: \diamond ; and experimental results: \circ , $t = 1.5s$; \triangleleft , $t = 3.0s$. Experimental results taken from Bouard & Coutanceau (1980).

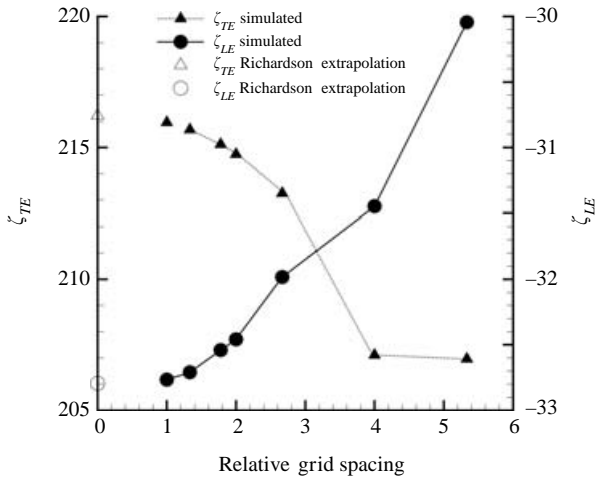


FIGURE 18. Vorticity at the leading edge (ζ_{LE}) and trailing edge (ζ_{TE}) for various grid resolutions. A relative grid spacing of 1 corresponds to a 512×512 grid.

are characterized by very strong gradients and are expected to be the most difficult to resolve.

Using the 512×512 , 384×384 and 288×288 grids, the order of convergence was calculated to be 2.48 at the leading edge and 3.82 at the trailing edge. Additionally, the convergence rate of the velocity at several points in the wake was computed to be between 2.0 and 3.0.

Note that the values for the 256×256 grid (relative grid spacing of 2) are within 1% of the theoretical solution at zero grid spacing and are well within the asymptotic range of convergence. Given the number of simulations needed for the parametric studies, this resolution was chosen as the best compromise between computational speed and accuracy.

Appendix B. Linear stability analysis

For parallel flows with a horizontal velocity profile $U(y)$, the linear stability of the flow is governed by the Orr–Sommerfeld equation:

$$\left\{ \left(\frac{d^2}{dy} - \alpha^2 \right)^2 - iRe \left[(\alpha U - \omega) \left(\frac{d^2}{dy} - \alpha^2 \right) - \alpha U'' \right] \right\} \phi = 0, \quad (\text{B } 1)$$

where the primes denote differentiation with respect to y . Disturbances are assumed to be of the form:

$$\hat{\psi} \equiv \phi(y) e^{-i(\alpha x - \omega t)},$$

where α is the (complex) wavenumber and ω the frequency of the disturbance. Thus, if the imaginary part of the wavenumber, α_i is negative, the disturbance will grow in space downstream.

Equation (B 1) is discretized using fourth-order finite differences and solved by choosing ω real and solving the resulting eigenvalue problem for α . Two hundred evenly spaced points in the wake were used for the profile $U(y)$ (no significant difference in solutions was found using 400 points).

REFERENCES

- AHMADI, A. R. & WIDNALL, S. E. 1985 Unsteady lifting-line theory as a singular-perturbation problem. *J. Fluid Mech.* **153**, 59–81.
- AHMADI, A. R. & WIDNALL, S. E. 1986 Energetics and optimum motion of oscillating lifting surfaces of finite span. *J. Fluid Mech.* **162**, 261–282.
- ANDERSON, J. M., STREITLIEN, K., BARRETT, K. S. & TRIANTAFYLLOU, M. S. 1998 Oscillating foils of high propulsive efficiency. *J. Fluid Mech.* **360**, 41–72.
- ARCHER, R. D., SAPPUPPO, J. & BETTERIDGE, D. J. 1979 Propulsive characteristics of flapping wings. *Aero. J.* **83**, 355–371.
- ASHLEY, S. 1998 Palm-size spy planes. *Mech. Engng* **120**, 74–78.
- BETTERIDGE, D. J. & ARCHER, R. D. 1974 A study of the mechanics of flapping flight. *Aero. Q.* **25**, 129–142.
- BETZ, A. 1912 Ein Beitrag zur Erklärung des Segelfluges. *Z. Flugtech. Motorluftschiff.* **3**, 269–272.
- BOUARD, R. & COUTANCEAU, M. 1980 The early stage of development of the wake behind an impulsively started cylinder for $40 < Re < 10^4$. *J. Fluid Mech.* **101**, 583–608.
- CHOPRA, M. G. 1974 Hydromechanics of lunate-tail swimming propulsion. *J. Fluid Mech.* **64**, 375–391.
- CHOPRA, M. G. 1976 Large amplitude lunate tail theory of fish locomotion. *J. Fluid Mech.* **74**, 161–182.
- CHOPRA, M. G. & KAMBE, T. 1977 Hydromechanics of lunate tail swimming propulsion. Part 2. *J. Fluid Mech.* **79**, 49–69.
- DICKINSON, M. H., LEHMANN, F.-O. & SANE, S. 1999 Wing rotation and the aerodynamic basis of insect flight. *Science* **284**, 1954–1960.
- ELLINGTON, C. P., VAN DEN BERG, C., WILLMOTT, A. P. & THOMAS, A. L. R. 1996 Leading-edge vortices in insect flight. *Nature* **384**, 626–630.
- FREYMUTH, P. 1985 The vortex patterns of dynamic separation: a parametric and comparative study. *Prog. Aerosp. Sci.* **22**, 161–208.
- FREYMUTH, P. 1988 Propulsive vortical signature of plunging and pitching airfoils. *AIAA J.* **26**, 881–883.
- GARRICK, I. E. 1936 Propulsion of a flapping and oscillating airfoil. *NACA TR* 567.
- GOPALKRISHNAN, R., TRIANTAFYLLOU, M. S., TRIANTAFYLLOU, G. S. & BARRETT, D. 1994 Active vorticity control in a shear flow using a flapping foil. *J. Fluid Mech.* **274**, 1–21.
- GUSTAFSON, K. 1996 Biological dynamical subsystems of hovering flight. *Maths Comput. Sim.* **40**, 397–410.

- GUSTAFSON, K. & LEBEN, R. R. 1988 Robust multigrid computation and visualization of separation and vortex evolution in aerodynamics flows. In *Proc. 1st National Fluid Dynamics Congress (AIAA/ASME/SIAM/APS)*, pp. 174–184. Washington, DC: AIAA.
- HALL, K. C. & HALL, S. R. 1996 Minimum induced power requirements for flapping flight. *J. Fluid Mech.* **323**, 285–315.
- HALL, K. C., PIGOTT, S. A. & HALL, S. R. 1998 Power requirements for large-amplitude flapping flight. *J. Aircraft* **35**, 352–361.
- JONES, K. D., DOHRING, C. M. & PLATZER, M. F. 1996 Wake structures behind plunging airfoils: a comparison of numerical and experimental results. *AIAA Paper* 96-0078. 34th AIAA Aerospace Sciences Meeting, Reno, NV.
- JONES, K. D., DOHRING, C. M. & PLATZER, M. F. 1998 Experimental and computational investigation of the Knoller–Betz effect. *AIAA J.* **37**, 1240–1246.
- JONES, K. D. & PLATZER, M. F. 1997 Numerical computation of flapping-wing propulsion and power extraction. *AIAA Paper* 97-0826.
- KATZ, J. & PLOTKIN, A. 1991 *Low-Speed Aerodynamics: From Wing Theory to Panel Methods*. McGraw-Hill.
- KATZMAYR, R. 1922 Effect of periodic changes of angle of attack on behavior of airfoils. Translation from “*Zeitschrift für Flugtechnik und Motorluftschiffahrt*”. *NACA TR* TM 147.
- KNOLLER, R. 1909 Die Gesetze des Lufrowiderstandes. *Flug- und Motortechnik* **3**, 1–7.
- KÖNIG, M., EISENLOHR, H. & ECKELMANN, H. 1990 The fine structure in the Strouhal–Reynolds number relationship of the laminar wake of a circular cylinder. *Phys. Fluids A* **2**, 1607–1614.
- KOOCHESFAHANI, M. M. 1989 Vortical patterns in the wake of an oscillating airfoil. *AIAA J.* **27**, 1200–1205.
- LAI, J. C. S. & PLATZER, M. F. 1999 Jet characteristics of a plunging airfoil. *AIAA J.* **37**, 1529–1537.
- LIGHTHILL, J. 1975 *Mathematical Biofluidynamics*, chap. 8. Society for Industrial and Applied Mathematics, Philadelphia.
- LIGHTHILL, M. J. 1969 Hydromechanics of aquatic animal propulsion. *Annu. Rev. Fluid Mech.* **1**, 413–446.
- LIGHTHILL, M. J. 1970 Aquatic animal propulsion of high hydromechanical efficiency. *J. Fluid Mech.* **44**, 265–301.
- LIU, H., ELLINGTON, C. P., KAWACHI, K., VAN DEN BERG, C. & WILLMOTT, A. P. 1998 A computational fluid dynamics study of hawkmoth hovering. *J. Expl Biol.* **201**, 461–477.
- LIU, P. & BOSE, N. 1997 Propulsive performance from oscillating propulsors with spanwise flexibility. *Proc. R. Soc. Lond. A* **453**, 1763–1770.
- MINOTTI, F. O. 2002 Unsteady two-dimensional theory of a flapping wing. *Phys. Rev. E* **66**, 051907.
- OBER, S. 1925 Note on the Katzmayr effect on airfoil drag. *NACA TR* TN 214.
- PEDLEY, T. J. & HILL, S. J. 1999 Large-amplitude undulatory fish swimming: fluid mechanics coupled to internal mechanics. *J. Expl Biol.* **202**, 3431–3438.
- PHILIPS, P. J., EAST, R. A. & PRATT, N. H. 1981 An unsteady lifting line theory of flapping wings with application to the forward flight of birds. *J. Fluid Mech.* **112**, 97–125.
- SANE, S. & DICKINSON, M. H. 2001 The control of flight force by a flapping wing: lift and drag production. *J. Expl Biol.* **204**, 2607–2626.
- SMITH, M. J. C. 1997 Reinstating inquiry into mechanized flapping-wing flight: realizing the integrity of the ornithopter. In *Proc. 35th Aerospace Sciences Meeting and Exhibit*, pp. 1–11. Reston, VA: AIAA.
- SMITH, M. J. C., WILKIN, P. J. & WILLIAMS, M. H. 1996 The advantages of an unsteady panel method in modeling the aerodynamic forces on rigid flapping wings. *J. Expl Biol.* **199**, 1073–1083.
- STREITLIEN, K., TRIANTAFYLLOU, G. S. & TRIANTAFYLLOU, M. S. 1996 Efficient foil propulsion through vortex control. *AIAA J.* **34**, 2315–2319.
- TANG, S. & AUBRY, N. 1997 On the symmetry breaking instability leading to vortex shedding. *Phys. Fluids* **9**, 2550–2561.
- THEODORSEN, T. 1935 General theory of aerodynamic instability and the mechanism of flutter. *NACA TR* 496.
- TRIANAFYLLOU, G. S., TRIANTAFYLLOU, M. S. & GROSENBAUGH, M. A. 1993 Optimal thrust development in oscillating foils with application to fish propulsion. *J. Fluid Struct.* **7**, 205–224.
- TRIANAFYLLOU, M. S. & TRIANTAFYLLOU, G. S. 1995 An efficient swimming machine. *Sci. Am.* **272**, 64–70.

- TRIANAFYLLOU, M. S., TRIANAFYLLOU, G. S. & YUE, D. K. P. 2000 Hydrodynamics of fishlike swimming. *Annu. Rev. Fluid Mech.* **32**, 33–53.
- TRITTON, D. J. 1959 Experiments on the flow past a circular cylinder at low Reynolds numbers. *J. Fluid Mech.* **6**, 547–567.
- TUNCER, I. H. & PLATZER, M. F. 1996 Thrust generation due to airfoil flapping. *AIAA J.* **34**, 324–331.
- WANG, Z. J. 2000 Vortex shedding and frequency selection in flapping flight. *J. Fluid Mech.* **410**, 323–341.
- WILLIAMSON, C. H. K. & ROSHKO, A. 1988 Vortex formation in the wake of an oscillating cylinder. *J. Fluids Struct.* **2**, 355–381.
- WILLMOTT, A. P. & ELLINGTON, C. P. 1997a Measuring the angle of attack of beating insect wings: robust three-dimensional reconstruction from two-dimensional images. *J. Expl Biol.* **200**, 2693–2704.
- WILLMOTT, A. P. & ELLINGTON, C. P. 1997b The mechanics of flight in the hawkmoth *manduca sexta* I. Kinematics of hovering and forward flight. *J. Expl Biol.* **200**, 2705–2722.
- WILLMOTT, P. 1988 Unsteady lifting-line theory by the method of matched asymptotic expansions. *J. Fluid Mech.* **186**, 303–320.
- WU, T. Y.-T. 1971 Hydromechanics of swimming propulsion. Part 1. Swimming of a two-dimensional flexible plate at variable forward speeds in an inviscid fluid. *J. Fluid Mech.* **46**, 337–355.
- ZHANG, H.-Q., FEY, U., NOACK, B. R., KÖNIG, M. & ECKELMANN, H. 1995 On the transition of the cylinder wake. *Phys. Fluids* **7**, 779–794.
- ZHU, Q., WOLFGANG, M. J., YUE, D. K. P. & TRIANAFYLLOU, M. S. 2002 Three-dimensional flow structures and vorticity control in fish-like swimming. *J. Fluid Mech.* **468**, 1–28.